Iodine Vacancies do not Cause Nonradiative Recombination in Halide Perovskites

Jingda Zhang,[1,‡,§] Xie Zhang,[2,*,‡] Mark E. Turiansky,[1] and Chris G. Van de Walle[1,†]

[1] *Materials Department, University of California, Santa Barbara, California 93106-5050, USA*

[2] *Beijing Computational Science Research Center, Beijing 100193, China*

(Received 7 December 2022; revised 22 February 2023; accepted 8 March 2023; published 24 March 2023)

The iodine vacancy (V_I) has frequently been discussed as a strong nonradiative recombination center in halide perovskites. This proposition was mainly based on the presence of charge-state transition levels in the band gap, as found in early first-principles calculations. In this work, we perform accurate hybrid-density-functional calculations for V_I in $CsPbI_3$, $CsSnI_3$, and $CsGeI_3$ and find that V_I does not have any transition levels in the band gap in $CsPbI_3$, in contrast to the results from calculations based on semilocal functionals. The iodine vacancy V_I does introduce levels in the band gap in $CsSnI_3$ and $CsGeI_3$, but our explicitly computed nonradiative capture coefficients demonstrate that V_I has a negligible impact on nonradiative recombination. Our study corrects a misunderstanding of the role of V_I in the iodide-based perovskites, and shifts the focus toward identifying and mitigating actual recombination centers in order to further improve the optoelectronic performance.

DOI: 10.1103/PRXEnergy.2.013008

I. INTRODUCTION

Despite the remarkable power conversion efficiencies (> 25% [1,2]) of perovskite solar cells, defect-assisted nonradiative recombination is still a key limitation for the photovoltaic performance of halide perovskites [3,4]. The identification of defects that act as strong nonradiative recombination centers is thus of critical importance.

Based on early calculations, the iodine vacancy (V_I) has often been considered as a nonradiative recombination center in halide perovskites (see, e.g., Refs. [5–7]). Experimentalists have even been developing strategies to passivate V_I [8,9]. The commonly employed theoretical approach to assessing if a defect is potentially a nonradiative recombination center is to inspect positions of its charge-state transition levels. The conventional wisdom suggests that if a defect has charge-state transition levels deep in the band gap, it is likely to cause strong nonradiative recombination [10,11].

Early first-principles calculations [12] based on density functional theory with the semilocal Perdew-Burke-Ernzerhof (PBE) [13] functional showed that V_I has no charge-state transition levels (i.e., the + charge state is always preferred) in the band gap in $MAPbI_3$ ($MA = CH_3NH_3$), and is thus not a recombination center. This result was later challenged by Agiorgousis *et al.* [5], who, with the same computational scheme, showed that V_I^- could significantly reduce its energy by forming a Pb-dimer configuration, leading to a $(+/-)$ transition level in the band gap. Similar observations were reported for V_I in $MASnI_3$ [14] and $CsGeI_3$ [6]. From there on, it has often been assumed that V_I acts as a nonradiative recombination center.

However, there are three major issues with this accepted wisdom. First, the use of the semilocal PBE functional is known to produce inaccurate defect properties in halide perovskites, though it yields more or less the right band gap due to an error cancelation if, simultaneously, spin-orbit coupling (SOC) is neglected [15]. In order to capture the correct defect physics, it is necessary to use hybrid functionals in conjunction with SOC [16]. Indeed, more recent calculations [17–19] have questioned the proposition of the iodine vacancies being a deep-level defect in $MAPbI_3$. Second, the presence of charge-state transition levels is a prerequisite for being a nonradiative recombination center, but does not guarantee that the defect will cause strong nonradiative recombination [20]; explicit computation of the nonradiative capture rates from first principles is essential [21,22]. Third, there is no experimental evidence supporting the role of iodine vacancies in

*xiezhang@csrc.ac.cn

†vandewalle@mrl.ucsb.edu

‡These authors contributed equally to this work.

§Present address: Department of Physics, National University of Singapore, 117551, Singapore

nonradiative recombination [23–25]; in fact, recent drive-level capacitance profiling experiments [26] indicated that iodine interstitials, rather than iodine vacancies, are the dominant nonradiative recombination centers.

In this work, we perform accurate first-principles calculations using the Heyd-Scuseria-Ernzerhof (HSE) [27] hybrid functional and including SOC to systematically assess the proposition that V_I acts as a nonradiative recombination center in representative halide perovskites, $CsPbI_3$, $CsSnI_3$, and $CsGeI_3$. To systematically study a set of materials, we focus on the all-inorganic compounds for consistency, but we explicitly checked that the MA molecule has a minor impact on the properties of V_I [28]. Experimentally, it has also been demonstrated that the organic cations have a minor impact on the recombination coefficients [29]. Hence, inspecting the properties of V_I in $CsPbI_3$, $CsSnI_3$, and $CsGeI_3$ is sufficient to capture the general trends in the iodide-based perovskites.

We use the orthorhombic perovskite phases for $CsPbI_3$ and $CsSnI_3$, and the rhombohedral phase for $CsGeI_3$, since they are energetically the most favorable perovskite phases and dynamically stable at room temperature. Our calculations show that V_I does not have any transition levels in the band gap in $CsPbI_3$, even if the Pb-dimer configuration is formed; the previous report of a $(+/-)$ transition level [5] was a consequence of the inaccurate computational scheme (PBE without SOC). The iodine vacancy V_I does introduce transition levels in the band gap in $CsSnI_3$ and $CsGeI_3$. However, the total nonradiative capture coefficient is negligibly small. We conclude that V_I is unlikely a nonradiative recombination center in the iodide-based perovskites. This insight is critical for the materials and device optimization of perovskite solar cells.

II. METHODS

A. First-principles calculations

The first-principles calculations in this study are based on density functional theory as implemented in the Vienna *ab initio* simulation package (VASP) [30]. We employ projector augmented-wave pseudopotentials [31] with a plane-wave energy cutoff of 500 eV and a $2 \times 2 \times 2$ ($3 \times 3 \times 3$) Γ-centered **k**-point grid for the orthorhombic perovskite (rhombohedral) unit cell of $CsPbI_3$ and $CsSnI_3$ ($CsGeI_3$). The HSE [27] hybrid functional is used and SOC is explicitly included. We use the experimental band gaps [32–34] as a benchmark criterion to determine the fraction of the nonlocal Fock exchange in the HSE functional (0.51 for $CsPbI_3$, 0.55 for $CsSnI_3$, and 0.38 for $CsGeI_3$); the screening parameter for the range separation is set to 0.2 $Å^{-1}$. With this setup, the calculated band gaps are 1.75 eV for $CsPbI_3$, 1.30 eV for $CsSnI_3$, and 1.60 eV for $CsGeI_3$. The computed electronic band structures also agree well with those obtained with the self-consistent *GW*+SOC approach [35]. The optimized lattice constants and their comparison with experimental measurements are listed in Table I.

TABLE I. Comparison between calculated and experimental lattice parameters. The values are expressed in angstroms.

Material	a_{calc}	b_{calc}	c_{calc}	a_{expt}	b_{expt}	c_{expt}
$CsPbI_3$	8.61	8.97	12.48	8.66 [32]	8.82 [32]	12.52 [32]
$CsSnI_3$	8.77	8.57	12.35	8.69 [33]	8.64 [33]	12.38 [33]
$CsGeI_3$	6.06	···	···	5.98 [34]	···	···

B. Defect formation energy

The formation energy of V_I in charge state q [$E^f(V_I^q)$] in a halide perovskite can be computed using the supercell approach as systematically described in Ref. [36], i.e.,

$$E^f(V_I^q) = E_{tot}(V_I^q) - E_{tot}(\text{bulk}) + \mu_I + qE_F + \Delta^q, \quad (1)$$

where $E_{tot}(V_I^q)$ and $E_{tot}(\text{bulk})$ are the total energies of the supercells of the halide perovskite with and without defect V_I^q. Here we employ a $2 \times 2 \times 1$ ($3 \times 3 \times 3$) supercell of the orthorhombic (rhombohedral) phase with 80 (135) atoms in total for $CsPbI_3$ and $CsSnI_3$ ($CsGeI_3$). We use the same energy cutoff and the equivalent **k**-point grid for the supercell calculations as those adopted for the unit cell. Here μ_I is the chemical potential of iodine, which we set to that corresponding to I-poor synthesis conditions; E_F is the Fermi level, referring to the chemical potential of electrons; Δ^q is a finite-size correction for charged defects, which is computed using the approach developed in Ref. [37].

C. Configuration coordinate diagram and nonradiative capture

Our formalism for computing the nonradiative capture coefficients is based on the so-called configuration coordinate diagram. We illustrate how the configuration coordinate diagram is constructed using a schematic example for a defect X with a $(+/0)$ charge-state transition level in the band gap [Fig. 1(a)]. In addition to the formation energies of defect X, the first-principles defect calculations also yield the equilibrium geometries of the defect in both 0 and + charge states. The configuration coordinate diagram probes how the potential energy surfaces of X^0 and X^+ evolve along the structural distortion pathway associated with the $X^+ \rightleftharpoons X^0$ charge-state transition. The structural distortion is characterized by a configuration coordinate difference (ΔQ), which is computed by

$$\Delta Q^2 = \sum_\alpha m_\alpha (\mathbf{R}_{\alpha;f} - \mathbf{R}_{\alpha;i})^2, \quad (2)$$

where m_α is the mass of atom α in the configurations of defect X; $\mathbf{R}_{\alpha;f}$ and $\mathbf{R}_{\alpha;i}$ are the Cartesian coordinates of atom α in the final and initial defect configurations.

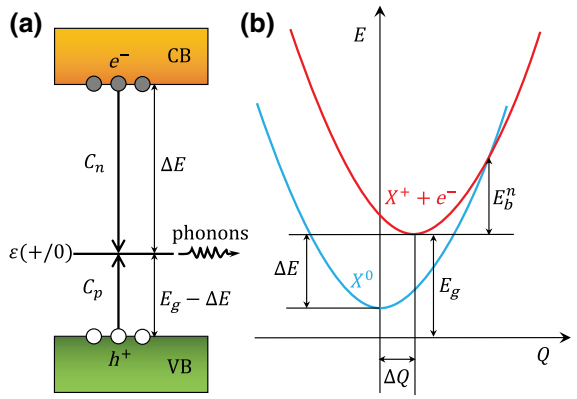

FIG. 1. (a) Schematic band diagram with a $(+/0)$ charge-state transition level of defect X in the band gap. Here ΔE ($E_g - \Delta E$) is the transition energy associated with electron (hole) capture, where E_g is the band gap. The filled (open) circles denote electrons (holes). (b) Schematic configuration coordinate diagram for electron capture by defect X^+. Here E_b^n is the electron capture barrier in a semiclassical picture.

As schematically depicted in Fig. 1(b), for the electron capture process by X^+, $Q = 0$ ($Q = \Delta Q$) refers to the equilibrium configuration of X^0 (X^+). By performing first-principles calculations for linearly interpolated structures between $Q = 0$ and $Q = \Delta Q$ (or extrapolated for the $Q < 0$ and $Q > \Delta Q$ regions), we obtain the potential energy surfaces as a function of the generalized configuration coordinate Q for both 0 and + charge states [see Fig. 1(b)]. Semiclassically, the electron capture process needs to overcome an energy barrier of E_b^n. Quantum mechanically, the nonradiative electron capture coefficient (C_n) can be computed based on Fermi's golden rule (see the detailed formulas in Refs. [38,39]). We calculate electron-phonon coupling matrix elements employing the linear-coupling approximation as implemented in VASP [30]. The overlap between the vibronic wave functions associated with the two anharmonic potential energy surfaces is computed by directly solving the one-dimensional Schrödinger equation [20,21] using the Fourier grid method [40].

D. Finite-temperature calculations

The phonons of V_I in three charge states (+, 0, and −) in $CsPbI_3$, $CsSnI_3$, and $CsGeI_3$ are computed using the finite displacement method as implemented in the Phonopy package [41]. The same supercell sizes as those used for defect calculations are employed for the phonon calculations. The forces are evaluated based on first-principles calculations with the computational setup described in Sec. II A. The vibrational free energies are obtained by integrating the vibrational frequencies over the Brillouin zone with a dense **q**-point grid of $30 \times 30 \times 30$.

To assess the impact of lattice vibrations on the band edges, we perform *ab initio* molecular dynamics (AIMD) simulations for bulk $CsPbI_3$, $CsSnI_3$, and $CsGeI_3$ supercells with the same sizes as those used for the defect calculations. We use the canonical (*NVT*) ensemble with the Nosé-Hoover [42,43] thermostat for temperature control. The AIMD simulations are carried out for 2000 steps with a time step of 1 fs. We perform an ensemble average for the band-edge levels obtained from the AIMD simulations.

III. RESULTS AND DISCUSSION

A. Defect formation energy

Figure 2(a) shows the formation energies of V_I in $CsPbI_3$ computed, on the one hand, using PBE without SOC or, on the other hand, HSE with SOC. As noted above, the two computational schemes yield very similar band gaps (1.82 eV for PBE versus 1.75 eV for HSE+SOC). However, the defect properties computed with the two schemes are clearly different. Even though the Pb-dimer configuration is favored for V_I^- in both cases [see the inset of Fig. 2(a)], there is no transition level in the band gap [the $(+/0)$ level is at 1.9 eV and the $(0/-)$ level at 2.0 eV above the valence-band maximum (VBM)] if we use the more accurate scheme based on a hybrid functional with inclusion of SOC. We can attribute this primarily to the fact that, on an absolute energy scale, the conduction-band minimum (CBM) shifts downwards in HSE+SOC relative to the PBE calculation. There are two contributions to this shift. First, the HSE functional tends to slightly increase the CBM and significantly decrease the VBM compared to the PBE functional. Second, the inclusion of SOC drastically reduces the CBM, since the CBM is dominated by Pb p states [44,45], with a SOC-splitting energy comparable to the band gap [46]. The net result is that the CBM exhibits a pronounced downward shift when switching from PBE to HSE+SOC, leading to the $(+/0)$ and $(0/-)$ transition levels now being above the CBM. This is also true for V_I in $MAPbI_3$ [28]. The iodine vacancy V_I is therefore not a nonradiative recombination center in $CsPbI_3$.

Figures 2(b) and 2(c) present the formation energies of V_I in $CsSnI_3$ and $CsGeI_3$. We observe a number of differences from the behavior of V_I in $CsPbI_3$. First, V_I^0 has a slightly lower formation energy in $CsSnI_3$ than in $CsPbI_3$. This is because V_I prefers the Sn-dimer configuration also in the neutral charge state, in contrast to the preference of V_I^0 in $CsPbI_3$ or $CsGeI_3$. We attribute this distinct behavior of V_I^0 to the fact that Sn vacancies (V_{Sn}) very easily form in $CsSnI_3$ (they have negative formation energies throughout the band gap, caused by Sn preferring the +4 oxidation state). This low-energy cost enables a Sn atom next to V_I to easily move off its substitutional site and form a Sn dimer. Second, V_I has much higher formation energies in $CsGeI_3$ than in $CsPbI_3$ or $CsSnI_3$. We attribute this difference to the fact that $CsGeI_3$ is most stable in the

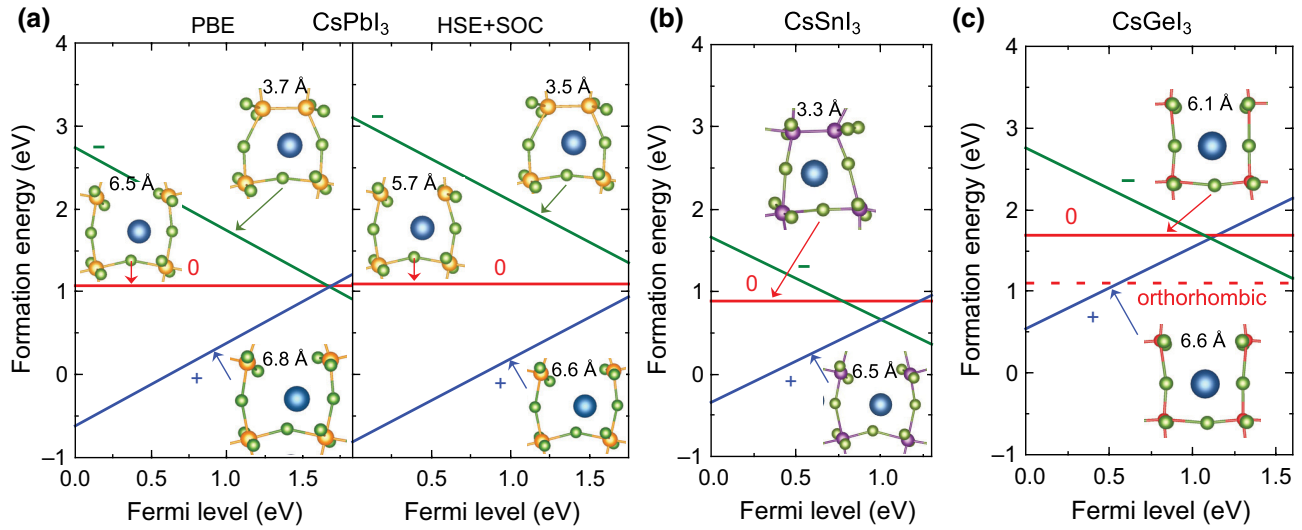

FIG. 2. Formation energy of V_I as a function of the Fermi level in $CsPbI_3$ (a), $CsSnI_3$ (b), and $CsGeI_3$ (c) under I-poor synthesis conditions. The left panel in (a) depicts the result computed using the PBE functional without SOC, while the right panels shows results for HSE with SOC. The red dashed line in (c) shows the formation energy of V_I^0 in orthorhombic $CsGeI_3$.

rhombohedral phase rather than the orthorhombic phase. If we compute the formation energy of V_I^0 in orthorhombic $CsGeI_3$ (while ensuring that the lattice stays within the orthorhombic perovskite structure), V_I^0 has an almost identical formation energy to that in $CsPbI_3$. Third, V_I has transition levels in the band gap for both $CsSnI_3$ and $CsGeI_3$, even if we use the accurate HSE+SOC scheme. This implies that V_I could potentially be a recombination center in $CsSnI_3$ and $CsGeI_3$, but the capture rates still need to be rigorously computed. We therefore perform a quantitative study of nonradiative capture by V_I in $CsSnI_3$ and $CsGeI_3$.

B. Nonradiative capture by V_I in $CsSnI_3$

Figure 3(a) shows the relaxed atomic structures of V_I^+, V_I^0, and V_I^- in $CsSnI_3$. In the + charge state, the two Sn neighbors of V_I are well separated. However, for both 0 and − charge states, the two Sn atoms move toward the vacancy site, forming a Sn dimer, and the Sn-Sn distance is reduced from 6.5 Å for V_I^+ to 3.3 Å for V_I^0 and 3.1 Å for V_I^-.

The V_I in $CsSnI_3$ is a "negative-U" center, meaning that the neutral charge state is never thermodynamically stable [see Fig. 2(b)]. However, the (+/−) thermodynamic transition level is not really relevant, since the likelihood of capturing two electrons or holes at once is extremely low [47]. We therefore focus on the (+/0) and (0/−) levels. As shown by the arrows and labels in Fig. 3(a), there exist four capture processes associated with the charge-state transitions of V_I in $CsSnI_3$. For instance, V_I^+ can capture an electron and transition to V_I^0, with a capture coefficient C_n^+; similarly, V_I^0 may capture a hole and go back to V_I^+, with a coefficient C_p^0. In this notation, the subscript denotes electron (n) or hole (p) capture, and the superscript represents the charge state of the initial configuration.

To examine the capture processes, we compute the potential energy surfaces of V_I as a function of a generalized configuration coordinate (Q) (see Sec. II C). Figure 3(b) shows the configuration coordinate diagram for the $V_I^+ \rightleftharpoons V_I^0$ transition in $CsSnI_3$. Here $Q = 0$ denotes the equilibrium configuration of V_I^0, and $Q = \Delta Q$ denotes that of V_I^+. Using the $V_I^+ \rightleftharpoons V_I^0$ transition as an example, we illustrate how a nonradiative capture cycle can be achieved. Beginning from V_I^+ with an electron at the CBM and a hole at the VBM [the green curve in Fig. 3(b)], V_I^+ may capture the electron from the CBM and transition to V_I^0 [the orange curve in Fig. 3(b)]. Within a semiclassical picture, this process needs to overcome an energy barrier [ΔE_n^+ in Fig. 3(b)]. In a similar manner, the hole can be captured by V_I^0, which allows V_I^0 to transition back to V_I^+ [the blue curve in Fig. 3(b)]. This capture process has an energy barrier that is almost zero.

According to the conventional wisdom, the capture coefficient decays exponentially with the transition energy (the energy difference between the transition level and the band edge from which the carrier is captured) [48], since the capture barrier increases with increasing transition energy. The (+/0) level is close to the CBM and thus we would expect the capture barrier to be small. However, the electron capture barrier is actually large, implying slow electron capture. This deviation from the conventional wisdom occurs because of the pronounced lattice relaxations associated with the $V_I^+ \rightleftharpoons V_I^0$ transition ($\Delta Q >$ 50 amu$^{1/2}$ Å). Consequently, the system is pushed into a regime where the potential energy surfaces intersect within

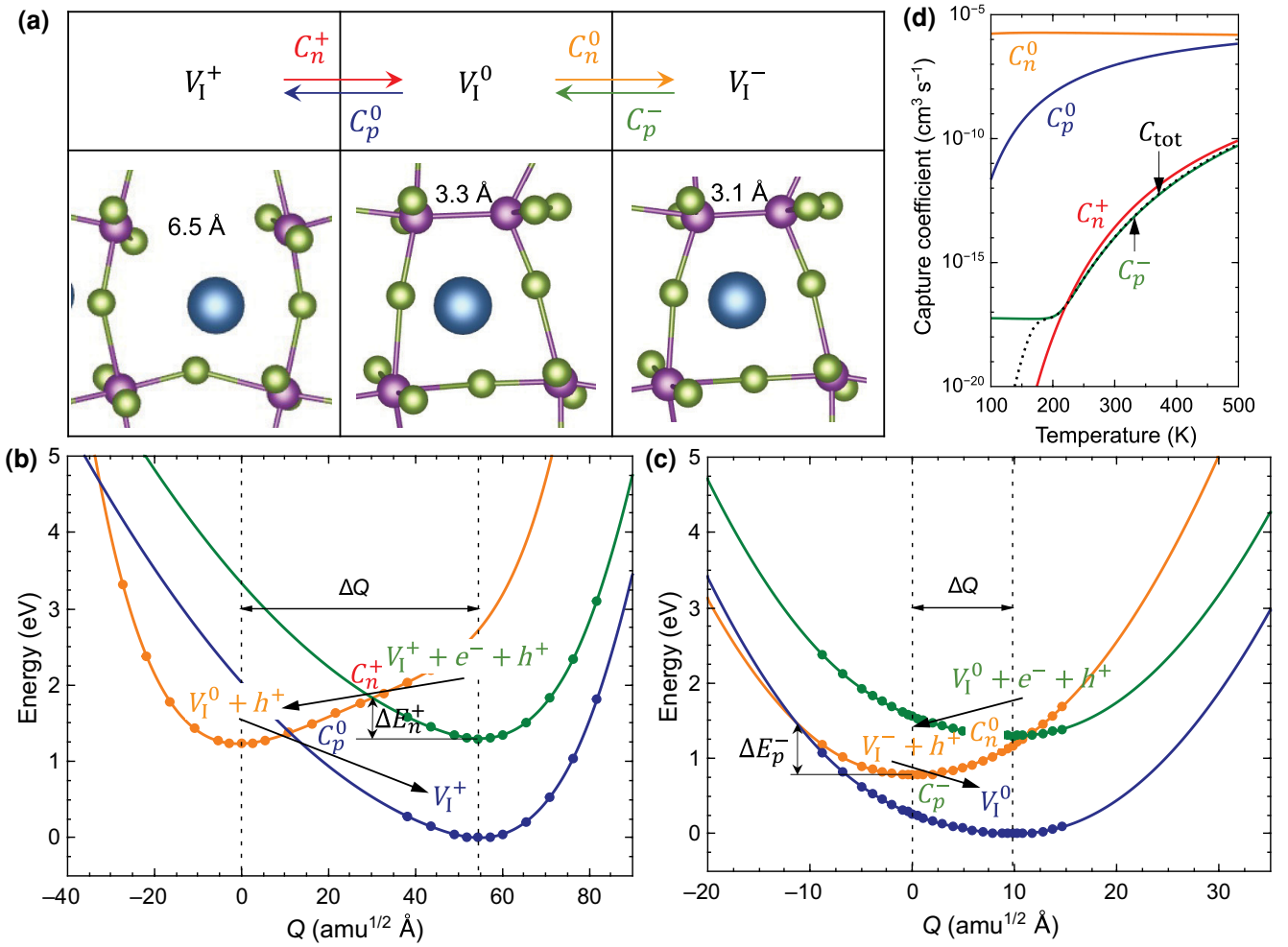

FIG. 3. (a) Local atomic structures of V_I in the +, 0, and − charge states and the four capture processes associated with the charge-state transitions in $CsSnI_3$. (b),(c) Configuration coordinate diagrams for the $V_I^+ \rightleftharpoons V_I^0$ (b) and $V_I^0 \rightleftharpoons V_I^-$ (c) charge-state transitions in $CsSnI_3$. (d) Nonradiative capture coefficients of V_I in $CsSnI_3$ as a function of temperature.

the interval $0 \le Q \le \Delta Q$ rather than for $Q > \Delta Q$ or $Q < 0$. In this case, the capture barrier no longer decreases with increasing transition energy. This indicates that judging the capture rates of a defect in halide perovskites (or in any system where the lattice relaxations induced by charge-state transitions are pronounced) based on the position of the transition level is problematic.

In the case of the $V_I^0 \rightleftharpoons V_I^-$ transition [see Fig. 3(c)], the change in lattice relaxations is much more modest. The electron capture barrier is small, but the hole capture barrier is large, which suggests fast electron capture and slow hole capture. To determine the total capture coefficient of V_I, we need to take all four capture processes into account. Under steady-state conditions, the total capture coefficient (C_{tot}) can be derived through a detailed balance of electron and hole capture [49], leading to

$$C_{tot} = \frac{C_n^0 + C_p^0}{1 + C_n^0/C_p^- + C_p^0/C_n^+}. \quad (3)$$

Each of the capture coefficients can be computed quantum mechanically using the multiphonon emission methodology as documented in Ref. [38] (see also Sec. II C).

Figure 3(d) shows the explicitly calculated capture coefficients for V_I in $CsSnI_3$. As implied already by the barrier heights, C_p^0 and C_n^0 are relatively high, but C_n^+ and C_p^- are fairly low. For most of the temperature window depicted in Fig. 3(d), C_n^0/C_p^- is larger than C_p^0/C_n^+ and both of them are much greater than 1. Hence, the denominator in Eq. (3) is governed by C_n^0/C_p^-; the numerator in Eq. (3) is approximately equal to C_n^0. The total capture coefficient C_{tot} is therefore controlled by C_p^-, which is what we observe in Fig. 3(d). At low temperatures, C_p^- becomes constant, and C_n^+ decreases rapidly with decreasing temperature, which is due to larger overlaps in the potential energy surfaces associated with C_p^- and thus stronger quantum tunneling; this causes C_p^0/C_n^+ to gradually become larger than C_n^0/C_p^-. The total capture coefficient C_{tot} is thus limited by C_n^+ at low temperatures.

At room temperature, the total capture coefficient of V_I in $CsSnI_3$ is 1.1×10^{-14} cm^3 s^{-1}. We can relate the total capture coefficient to the overall nonradiative recombination coefficient A by multiplying with the defect concentration N_{def}, i.e., $A = N_{def}C_{tot}$; the nonradiative recombination rate in a device can then be obtained by multiplying A with the carrier density. Even if we assume an unrealistically high defect concentration of 10^{20} cm^{-3}, A is only around 10^6 s^{-1}; the corresponding lifetime is 1 μs ($\tau = 1/A$), which has a negligible impact on the device performance [3]. We thus conclude that V_I is not a strong nonradiative recombination center in $CsSnI_3$.

C. Nonradiative capture by V_I in $CsGeI_3$

We can similarly analyze the nonradiative capture by V_I in $CsGeI_3$. Despite qualitative differences in the atomic structure of V_I^0 in $CsGeI_3$ versus $CsSnI_3$, the charge-state transitions in $CsGeI_3$ are still $V_I^+ \rightleftharpoons V_I^0 \rightleftharpoons V_I^-$, which involve two electron capture and two hole capture processes [see Fig. 4(a)]. The similar atomic structures of V_I^+ and V_I^0 in $CsGeI_3$ result in minor lattice relaxations (small ΔQ) and weak anharmonicity in the potential energy surfaces [see Fig. 4(b)]. Therefore, the electron capture barrier for the $V_I^+ \rightleftharpoons V_I^0$ transition is small, and the hole capture barrier is large, consistent with the (+/0) level being close to the CBM. In contrast, the transition between V_I^0 and V_I^- is accompanied by large lattice relaxations. The (0/−) transition level of V_I is close to the midgap, and both the electron and hole capture barriers are large and similar in magnitude [see Fig. 4(c)].

The resulting capture coefficients for V_I in $CsGeI_3$ are shown in Fig. 4(d). As expected from the large barriers, C_n^0 and C_p^- are extremely low. Coefficient C_p^0 is higher than C_n^0 and C_p^-, but still very low on an absolute scale. Only C_n^+ is high, of the order of 10^{-8}–10^{-7} cm^3 s^{-1}. One can easily show that the numerator in Eq. (3) is dominated by

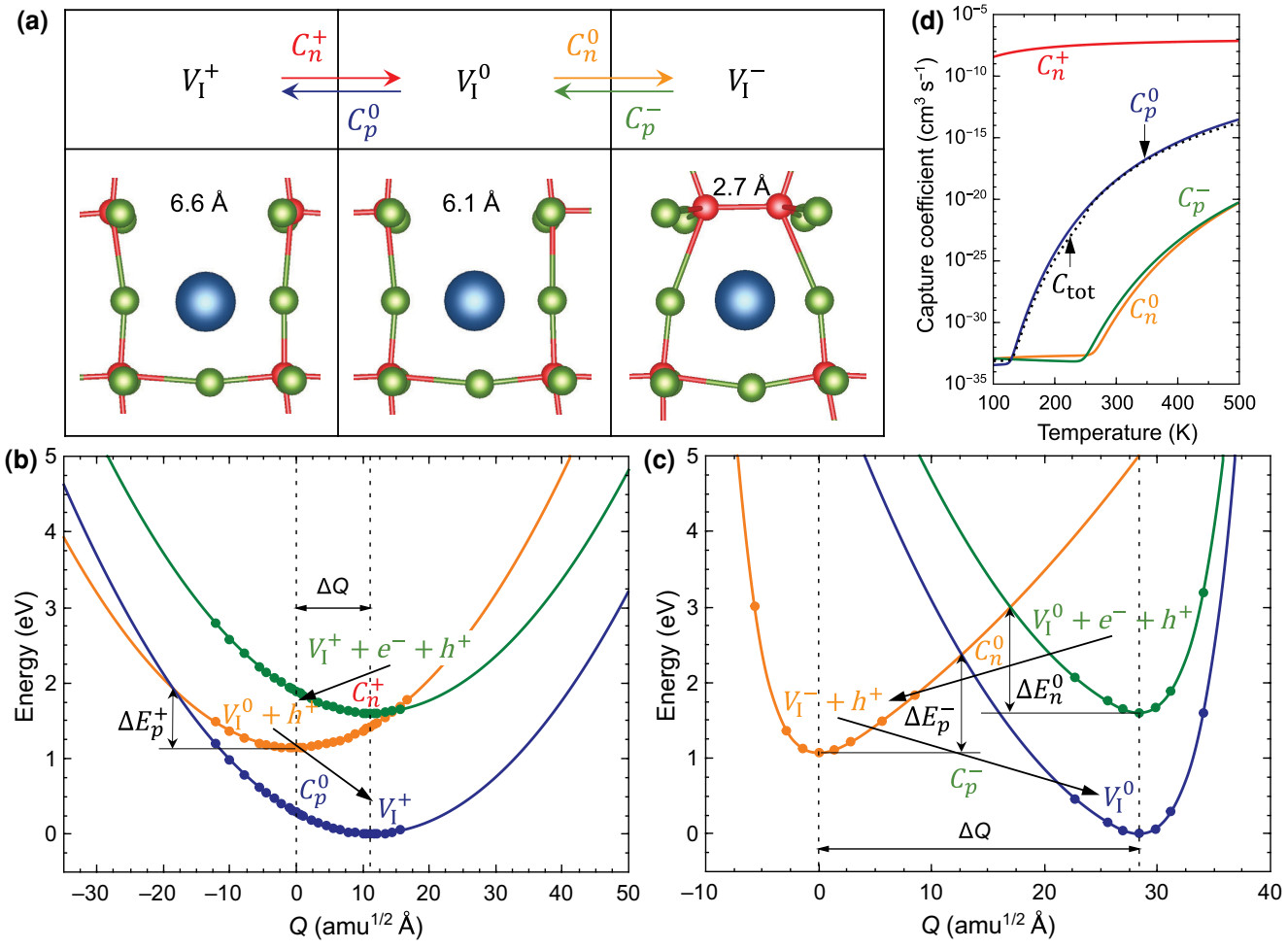

FIG. 4. (a) Local atomic structures of V_I in the +, 0, and − charge states and the four capture processes associated with the charge-state transitions in $CsGeI_3$. (b),(c) Configuration coordinate diagrams for the $V_I^+ \rightleftharpoons V_I^0$ (b) and $V_I^0 \rightleftharpoons V_I^-$ (c) charge-state transitions in $CsGeI_3$. (d) Nonradiative capture coefficients of V_I in $CsGeI_3$ as a function of temperature.

C_p^0 and the denominator is roughly equal to 2. Hence, C_{tot} is controlled by C_p^0 [see also Fig. 4(d)].

At room temperature, the total capture coefficient of V_I in $CsGeI_3$ is 3.2×10^{-19} cm^3 s^{-1}, which is 5 orders of magnitude lower than that of V_I in $CsSnI_3$. In addition, the formation energy of V_I is higher in $CsGeI_3$ than in $CsSnI_3$, implying a lower density. Therefore, we conclude that V_I is not a nonradiative recombination center in $CsGeI_3$ either.

D. Impact of lattice vibrations

There have been reports in the literature that lattice vibrations may have a critical impact on the defect properties of halide perovskites. For instance, the Kohn-Sham level associated with the bromine vacancy (V_{Br}) in $CsPbBr_3$ was found to exhibit large fluctuations (up to 1 eV) at room temperature [50]. To assess the impact of lattice vibrations on the properties of V_I, we perform AIMD simulations for V_I in $CsPbI_3$ with the PBE functional.

Figure 5 shows the thermal fluctuation of the Kohn-Sham level associated with V_I in $CsPbI_3$ at room temperature. Different from the case of V_{Br} in $CsPbBr_3$, the thermal fluctuation is much smaller, i.e., only of the order of ± 0.1 eV. Furthermore, we find that once SOC has been included (for either the PBE or HSE functional), the CBM shifts downwards and the Kohn-Sham level associated with V_I becomes higher than the CBM.

Still, we note that the electronic behavior of a defect is governed by the charge-state transition level, not by the Kohn-Sham level, which is calculated for a specific charge state; structural relaxations associated with the charge-state transition can have an important effect. To examine the effect of lattice vibrations on the charge-state transition levels of V_I, we explicitly compute the phonons and thus the vibrational free energies of V_I in different charge states

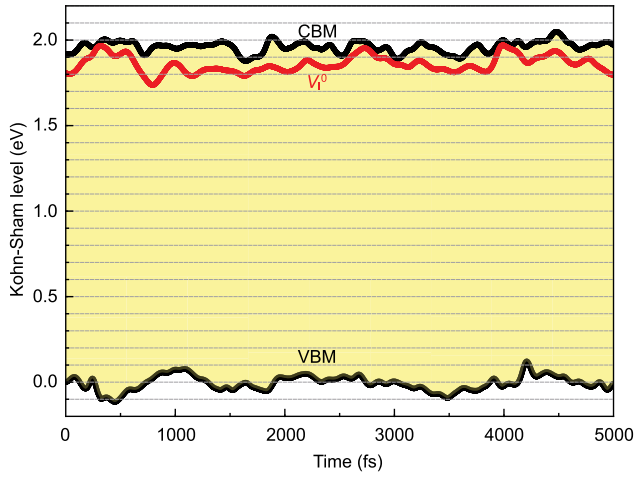

FIG. 5. Thermal fluctuations of the band edges and the Kohn-Sham level associated with V_I^0 in $CsPbI_3$ obtained from AIMD simulations at room temperature using the PBE functional.

(+, 0, and −) in all three compounds ($CsPbI_3$, $CsSnI_3$, and $CsGeI_3$). We further take into account the impact of lattice vibrations on the band edges by performing an ensemble average for the VBM and CBM levels from AIMD simulations of bulk $CsPbI_3$, $CsSnI_3$, and $CsGeI_3$ at finite temperatures.

Figure 6 shows the temperature dependence of the charge-state transition levels of V_I and band edges in $CsPbI_3$, $CsSnI_3$, and $CsGeI_3$. In all cases, the $(+/0)$ and $(0/-)$ charge-state transition levels themselves change only slightly (± 0.1 eV) between 0 K and room temperature. In $CsPbI_3$ and $CsGeI_3$, the band edges also display only small shifts. The only notable effect occurs in the VBM of $CsSnI_3$, which does exhibit a downshift (about 0.23 eV from $T = 0$ to $T = 300$ K).

To understand how these changes in the transition energies impact the nonradiative capture barriers, we reevaluate the configuration coordinate diagrams for the $V_I^+ \rightleftharpoons V_I^0$ and $V_I^0 \rightleftharpoons V_I^-$ transitions in $CsSnI_3$ and $CsGeI_3$, taking into account the shifts in the transition levels and band edges at room temperature (see the Supplemental Material [51] for details). We find that the rate-limiting capture barriers remain large or become even greater. Temperature could in principle also impact the *shape* of the potential energy surfaces; however, our findings about the small size of the fluctuations in the defect levels give us confidence that these effects will be small. Our analysis thus indicates that large capture barriers will persist, and our conclusions remain qualitatively unchanged: the iodine vacancies are highly unlikely to act as nonradiative recombination centers.

E. Discussion

Recent experimental studies have recognized the importance of defect control in order to further improve the performance of halide perovskite solar cells and light emitters. Passivation of nonradiative recombination centers has been an active research topic, and knowing the microscopic nature of the detrimental defects is crucial for that effort. Most of these studies (see, e.g., Refs. [52–55]) have hypothesized that the defect of concern is V_I. This was largely motivated by the fact that V_I has low formation energies, and previous calculations [5,6,14] suggested that V_I is a deep-level defect and potentially a strong nonradiative recombination center.

Our present study demonstrates, however, that V_I is not a defect of concern. In $CsPbI_3$, V_I does not have charge-state transition levels in the band gap; previous studies that reached other conclusions were less reliable because of the use of the semilocal PBE functional and the omission of SOC. In $CsSnI_3$ and $CsGeI_3$, V_I does introduce deep levels in the band gap, but our rigorous evaluation of nonradiative capture rates shows that it does not cause strong nonradiative recombination.

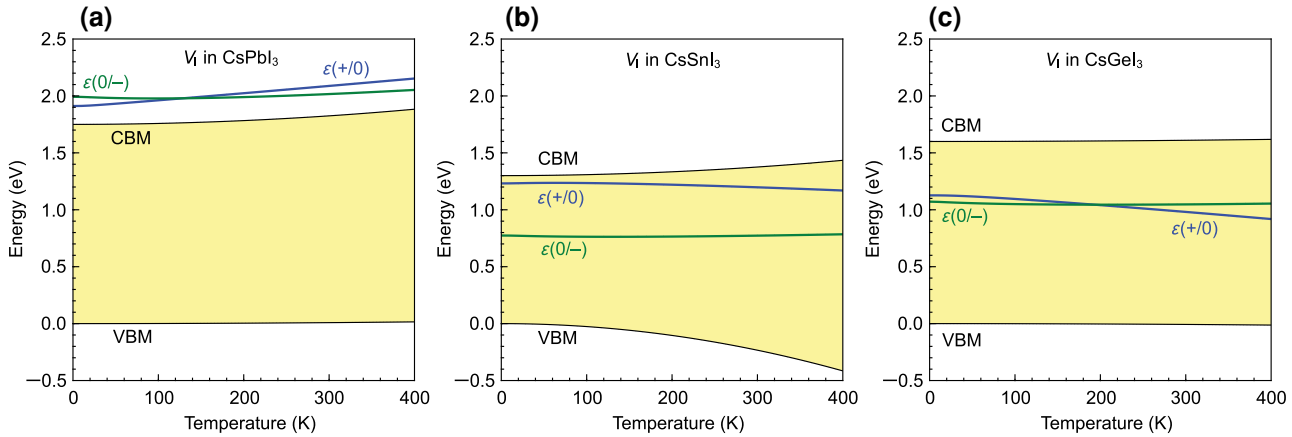

FIG. 6. Temperature dependence of the charge-state transition levels of V_I and band edges in (a) $CsPbI_3$, (b) $CsSnI_3$, and (c) $CsGeI_3$.

Our systematic study focused on the all-inorganic compounds, but we have evidence that the conclusions apply to hybrid perovskites as well. A comparison between the properties of defects in $MAPbI_3$ [28] and $CsPbI_3$ [56] showed that the organic cations may introduce additional "intramolecular" defects such as hydrogen vacancies, but their presence has a minor impact on the properties of other intrinsic defects. The same conclusion applies to $FAPbI_3$ [FA = $CH(NH_2)_2$] [57]. We can therefore generalize our result and conclude that V_I is unlikely to be a nonradiative recombination center in either all-inorganic or hybrid iodide perovskites.

Our calculations have focused on specific phases of the three perovskite compounds. It was experimentally shown that the nonradiative capture rates in the higher-temperature cubic phase might be slightly higher (by a factor of 2, at comparable temperatures) [58]. Carrying out explicit defect calculations for the cubic phases is technically challenging because they are dynamically unstable at 0 K; developing new approaches to obtain nonradiative capture coefficients in such phases would be desirable. Nevertheless, our own calculations of rates for defects in different phases, combined with the experimental evidence regarding the impact of the phase on rates in Ref. [58], indicate that the phase will only have a minor impact on the nonradiative capture coefficients. Since our calculated nonradiative recombination rates for iodine vacancies are *many orders of magnitude* smaller than expected for efficient recombination centers, we conclude that iodine vacancies do not cause nonradiative recombination.

IV. CONCLUSIONS

To summarize, we have systematically shown that the iodine vacancy is *not* a nonradiative recombination center in the iodide-based perovskites. This negates a common belief in the field that the iodine vacancy causes strong nonradiative losses and should be passivated. Previous first-principles calculations that supported this belief suffered from either an inaccurate level of theory or a lack of rigorous computations for the nonradiative capture coefficients. We note that the iodine vacancy may still trap or scatter carriers, which reduces doping efficiency or mobility; the hysteresis observed in experiments [59] may also be caused by the iodine vacancies. These effects might still impact the device performance, but our central point here is that the iodine vacancy is not a nonradiative recombination center. Future efforts to suppress the detrimental nonradiative recombination centers should be focused on the centers that are actually important, such as the iodine interstitial [21,56], in order to push the performance of halide perovskites toward the Shockley-Queisser efficiency limit.

ACKNOWLEDGMENTS

X.Z. is supported by the National Natural Science Foundation of China (Grants No. 52172136 and No. U2230402). M.E.T. and C.G.VdW. are supported by the U.S. Department of Energy (DOE), Office of Science, Basic Energy Sciences (BES) under Award No. DE-SC0010689. Computational resources were provided by the National Energy Research Scientific Computing Center, a DOE Office of Science User Facility supported by the Office of Science of the U.S. Department of Energy under Contract No. DE-AC02-05CH11231.

[1] J. Jeong, *et al.*, Pseudo-halide anion engineering for α-$FAPbI_3$ perovskite solar cells, Nature **592**, 381 (2021).
[2] Y. Zhao, F. Ma, Z. Qu, S. Yu, T. Shen, H.-X. Deng, X. Chu, X. Peng, Y. Yuan, X. Zhang, and J. You, Inactive $(PbI_2)_2RbCl$ stabilizes perovskite films for efficient solar cells, Science **377**, 531 (2022).
[3] X. Zhang, J.-X. Shen, and C. G. Van de Walle, First-principles simulation of carrier recombination mechanisms

in halide perovskites, Adv. Energy Mater. **10**, 1902830 (2020).
[4] H. Jin, E. Debroye, M. Keshavarz, I. G. Scheblykin, M. B. J. Roeffaers, J. Hofkens, and J. A. Steele, It's a trap! On the nature of localised states and charge trapping in lead halide perovskites, Mater. Horiz. **7**, 397 (2020).
[5] M. L. Agiorgousis, Y.-Y. Sun, H. Zeng, and S. Zhang, Strong covalency-induced recombination centers in perovskite solar cell material $CH_3NH_3PbI_3$, J. Am. Chem. Soc. **136**, 14570 (2014).
[6] W. Ming, H. Shi, and M.-H. Du, Large dielectric constant, high acceptor density, and deep electron traps in perovskite solar cell material $CsGeI_3$, J. Mater. Chem. A **4**, 13852 (2016).
[7] X. Xu, Z. Wu, Z. Zhao, Z. Lu, Y. Gao, X. Huang, J. Huang, Z. Zhang, Y. Cai, Y. Qu, N. Cui, W. Xie, T. Shi, and P. Liu, First-principles study of detrimental iodine vacancy in lead halide perovskite under strain and electron injection, Appl. Phys. Lett. **121**, 092106 (2022).
[8] M. Abdi-Jalebi, Z. Andaji-Garmaroudi, S. Cacovich, C. Stavrakas, B. Philippe, J. M. Richter, M. Alsari, E. P. Booker, E. M. Hutter, A. J. Pearson, S. Lilliu, T. J. Savenije, H. Rensmo, G. Divitini, C. Ducati, R. H. Friend, and S. D. Stranks, Maximizing and stabilizing luminescence from halide perovskites with potassium passivation, Nature **555**, 497 (2018).
[9] B. Chen, P. N. Rudd, S. Yang, Y. Yuan, and J. Huang, Imperfections and their passivation in halide perovskite solar cells, Chem. Soc. Rev. **48**, 3842 (2019).
[10] W. Shockley and W. T. Read, Statistics of the recombinations of holes and electrons, Phys. Rev. **87**, 835 (1952).
[11] R. N. Hall, Electron-hole recombination in germanium, Phys. Rev. **87**, 387 (1952).
[12] W.-J. Yin, T. Shi, and Y. Yan, Unusual defect physics in $CH_3NH_3PbI_3$ perovskite solar cell absorber, Appl. Phys. Lett. **104**, 063903 (2014).
[13] J. P. Perdew, K. Burke, and M. Ernzerhof, Generalized Gradient Approximation Made Simple, Phys. Rev. Lett. **77**, 3865 (1996).
[14] D. Meggiolaro, D. Ricciarelli, A. A. Alasmari, F. A. S. Alasmary, and F. De Angelis, Tin versus lead redox chemistry modulates charge trapping and self-doping in tin/lead iodide perovskites, J. Phys. Chem. Lett. **11**, 3546 (2020).
[15] X. Zhang, M. E. Turiansky, J.-X. Shen, and C. G. Van de Walle, Defect tolerance in halide perovskites: A first-principles perspective, J. Appl. Phys. **131**, 090901 (2022).
[16] J. Kang, Effects of band edge positions on defect structure in lead halide perovskites: A case study on the Br vacancy in $CsPbBr_3$, Phys. Rev. Mater. **4**, 085405 (2020).
[17] M.-H. Du, Density functional calculations of native defects in $CH_3NH_3PbI_3$: Effects of spin-orbit coupling and self-interaction error, J. Phys. Chem. Lett. **6**, 1461 (2015).
[18] D. Meggiolaro, S. G. Motti, E. Mosconi, A. J. Barker, J. Ball, C. Andrea Riccardo Perini, F. Deschler, A. Petrozza, and F. De Angelis, Iodine chemistry determines the defect tolerance of lead-halide perovskites, Energy Environ. Sci. **11**, 702 (2018).
[19] L. D. Whalley, P. van Gerwen, J. M. Frost, S. Kim, S. N. Hood, and A. Walsh, Giant Huang–Rhys factor for electron capture by the iodine intersitial in perovskite solar cells, J. Am. Chem. Soc. **143**, 9123 (2021).
[20] X. Zhang, M. E. Turiansky, and C. G. Van de Walle, Correctly assessing defect tolerance in halide perovskites, J. Phys. Chem. C **124**, 6022 (2020).
[21] X. Zhang, M. E. Turiansky, J.-X. Shen, and C. G. Van de Walle, Iodine interstitials as a cause of nonradiative recombination in hybrid perovskites, Phys. Rev. B **101**, 140101(R) (2020).
[22] X. Zhang, J.-X. Shen, M. E. Turiansky, and C. G. Van de Walle, Hidden role of Bi incorporation in nonradiative recombination in methylammonium lead iodide, J. Mater. Chem. A **8**, 12964 (2020).
[23] S. Reichert, Q. An, Y.-W. Woo, A. Walsh, Y. Vaynzof, and C. Deibel, Probing the ionic defect landscape in halide perovskite solar cells, Nat. Commun. **11**, 6098 (2020).
[24] S. Tan, I. Yavuz, M. H. Weber, T. Huang, C.-H. Chen, R. Wang, H.-C. Wang, J. H. Ko, S. Nuryyeva, J. Xue, Y. Zhao, K.-H. Wei, J.-W. Lee, and Y. Yang, Shallow iodine defects accelerate the degradation of α-phase formamidinium perovskite, Joule **4**, 2426 (2020).
[25] R. Wang, J. Xue, X. Chen, C. Yao, Z.-K. Wang, M. H. Weber, A. H. Rose, S. Nuryyeva, J. Zhu, T. Huang, Y. Zhao, S. Tan, M. C. Beard, Y. Yan, K. Zhu, and Y. Yang, Unraveling the surface state of photovoltaic perovskite thin film, Matter **4**, 2417 (2021).
[26] Z. Ni, H. Jiao, C. Fei, H. Gu, S. Xu, Z. Yu, G. Yang, Y. Deng, Q. Jiang, Y. Liu, Y. Yan, and J. Huang, Evolution of defects during the degradation of metal halide perovskite solar cells under reverse bias and illumination, Nat. Energy **7**, 65 (2022).
[27] J. Heyd, G. E. Scuseria, and M. Ernzerhof, Hybrid functionals based on a screened Coulomb potential, J. Chem. Phys. **118**, 8207 (2003).
[28] X. Zhang, J.-X. Shen, M. E. Turiansky, and C. G. Van de Walle, Minimizing hydrogen vacancies to enable highly efficient hybrid perovskites, Nat. Mater. **20**, 971 (2021).
[29] H. Zhu, M. T. Trinh, J. Wang, Y. Fu, P. P. Joshi, K. Miyata, S. Jin, and X. Y. Zhu, Organic cations might not be essential to the remarkable properties of band edge carriers in lead halide perovskites, Adv. Mater. **29**, 1603072 (2017).
[30] G. Kresse and J. Furthmüller, Efficient iterative schemes for ab initio total-energy calculations using a plane-wave basis set, Phys. Rev. B **54**, 11169 (1996).
[31] P. E. Blöchl, Projector augmented-wave method, Phys. Rev. B **50**, 17953 (1994).
[32] B. Zhao, S.-F. Jin, S. Huang, N. Liu, J.-Y. Ma, D.-J. Xue, Q. Han, J. Ding, Q.-Q. Ge, Y. Feng, and J.-S. Hu, Thermodynamically stable orthorhombic γ-$CsPbI_3$ thin films for high-performance photovoltaics, J. Am. Chem. Soc. **140**, 11716 (2018).
[33] I. Chung, J.-H. Song, J. Im, J. Androulakis, C. D. Malliakas, H. Li, A. J. Freeman, J. T. Kenney, and M. G. Kanatzidis, $CsSnI_3$: semiconductor or metal? High electrical conductivity and strong near-infrared photoluminescence from a single material. High hole mobility and phase-transitions, J. Am. Chem. Soc. **134**, 8579 (2012).
[34] C. C. Stoumpos, L. Frazer, D. J. Clark, Y. S. Kim, S. H. Rhim, A. J. Freeman, J. B. Ketterson, J. I. Jang, and M. G. Kanatzidis, Hybrid germanium iodide perovskite semiconductors: Active lone pairs, structural distortions, direct and indirect energy gaps, and strong nonlinear optical properties, J. Am. Chem. Soc. **137**, 6804 (2015).

[35] F. Brivio, K. T. Butler, A. Walsh, and M. van Schilfgaarde, Relativistic quasiparticle self-consistent electronic structure of hybrid halide perovskite photovoltaic absorbers, Phys. Rev. B **89**, 155204 (2014).

[36] C. Freysoldt, B. Grabowski, T. Hickel, J. Neugebauer, G. Kresse, A. Janotti, and C. G. Van de Walle, First-principles calculations for point defects in solids, Rev. Mod. Phys. **86**, 253 (2014).

[37] C. Freysoldt, J. Neugebauer, and C. G. Van de Walle, Fully Ab Initio Finite-Size Corrections for Charged-Defect Supercell Calculations, Phys. Rev. Lett. **102**, 016402 (2009).

[38] A. Alkauskas, Q. Yan, and C. G. Van de Walle, First-principles theory of nonradiative carrier capture via multiphonon emission, Phys. Rev. B **90**, 075202 (2014).

[39] M. E. Turiansky, A. Alkauskas, M. Engel, G. Kresse, D. Wickramaratne, J.-X. Shen, C. E. Dreyer, and C. G. Van de Walle, Nonrad: Computing nonradiative capture coefficients from first principles, Comput. Phys. Commun. **267**, 108056 (2021).

[40] C. C. Marston and G. G. Balint-Kurti, The Fourier grid Hamiltonian method for bound state eigenvalues and eigenfunctions, J. Chem. Phys. **91**, 3571 (1989).

[41] A. Togo and I. Tanaka, First principles phonon calculations in materials science, Scr. Mater. **108**, 1 (2015).

[42] S. Nosé, A unified formulation of the constant temperature molecular dynamics methods, J. Chem. Phys. **81**, 511 (1984).

[43] W. G. Hoover, Canonical dynamics: Equilibrium phase-space distributions, Phys. Rev. A **31**, 1695 (1985).

[44] X. Zhang, J.-X. Shen, and C. G. Van de Walle, Three-dimensional spin texture in hybrid perovskites and its impact on optical transitions, J. Phys. Chem. Lett. **9**, 2903 (2018).

[45] X. Zhang, J.-X. Shen, W. Wang, and C. G. Van de Walle, First-principles analysis of radiative recombination in lead-halide perovskites, ACS Energy Lett. **3**, 2329 (2018).

[46] J.-X. Shen, X. Zhang, S. Das, E. Kioupakis, and C. G. Van de Walle, Unexpectedly strong Auger recombination in halide perovskites, Adv. Energy Mater. **8**, 1801027 (2018).

[47] N. Bagraev and V. Mashkov, A mechanism for two-electron capture at deep level defects in semiconductors, Solid State Commun. **65**, 1111 (1988).

[48] C. H. Henry and D. V. Lang, Nonradiative capture and recombination by multiphonon emission in GaAs and GaP, Phys. Rev. B **15**, 989 (1977).

[49] A. Alkauskas, C. E. Dreyer, J. L. Lyons, and C. G. Van de Walle, Role of excited states in Shockley-Read-Hall recombination in wide-band-gap semiconductors, Phys. Rev. B **93**, 201304 (2016).

[50] A. V. Cohen, D. A. Egger, A. M. Rappe, and L. Kronik, Breakdown of the static picture of defect energetics in halide perovskites: the case of the br vacancy in $CsPbBr_3$, J. Phys. Chem. Lett. **10**, 4490 (2019).

[51] See Supplemental Material at http://link.aps.org/supplemental/10.1103/PRXEnergy.2.013008 for details of the configuration coordinate diagrams for V_I in $CsSnI_3$ and $CsGeI_3$ at room temperature.

[52] E. Aydin, M. Bastiani, and S. Wolf, Defect and contact passivation for perovskite solar cells, Adv. Mater. **31**, 1900428 (2019).

[53] L. Fu, H. Li, L. Wang, R. Yin, B. Li, and L. Yin, Defect passivation strategies in perovskites for an enhanced photovoltaic performance, Energy Environ. Sci. **13**, 4017 (2020).

[54] F. Gao, Y. Zhao, X. Zhang, and J. You, Recent progresses on defect passivation toward efficient perovskite solar cells, Adv. Energy Mater. **10**, 1902650 (2020).

[55] S. Akin, N. Arora, S. M. Zakeeruddin, M. Grätzel, R. H. Friend, and M. I. Dar, New strategies for defect passivation in high-efficiency perovskite solar cells, Adv. Energy Mater. **10**, 1903090 (2020).

[56] X. Zhang, M. E. Turiansky, and C. G. Van de Walle, All-inorganic halide perovskites as candidates for efficient solar cells, Cell Rep. Phys. Sci. **2**, 100604 (2021).

[57] X. Zhang and S.-H. Wei, Origin of Efficiency Enhancement by Lattice Expansion in Hybrid-Perovskite Solar Cells, Phys. Rev. Lett. **128**, 136401 (2022).

[58] R. L. Milot, G. E. Eperon, H. J. Snaith, M. B. Johnston, and L. M. Herz, Temperature-dependent charge-carrier dynamics in $CH_3NH_3PbI_3$ perovskite thin films, Adv. Funct. Mater. **25**, 6218 (2015).

[59] G. E. Eperon, G. M. Paternò, R. J. Sutton, A. Zampetti, A. A. Haghighirad, F. Cacialli, and H. J. Snaith, Inorganic caesium lead iodide perovskite solar cells, J. Mater. Chem. A **3**, 19688 (2015).